Immunomagnetic nanoscreening of circulating tumor cells with a motion controlled microfluidic system

Yu-yen Huang · Kazunori Hoshino · Peng Chen · Chun-hsien Wu · Nancy Lane · Michael Huebschman · Huaying Liu · Konstantin Sokolov · Jonathan W. Uhr · Eugene P. Frenkel · John X.J. Zhang

Abstract Combining the power of immunomagnetic assay and microfluidic microchip operations, we successfully detected rare CTCs from clinical blood samples. The microfluidic system is operated in a flip-flop mode, where a computer-controlled rotational holder with an array of microfluidic chips inverts the microchannels. We have demonstrated both theoretically and experimentally that the direction of red blood cell (RBC) sedimentation with regards to the magnetic force required for cell separation is important for capture efficiency, throughput, and purity. The flip-flop operation reduces the stagnation of RBCs and non-specific binding on the capture surface by alternating the direction of the magnetic field with respect to gravity. The developed immunomagnetic microchip-based screening system exhibits high capture rates (more than 90%) for SkBr3, PC3, and Colo205 cell lines in spiked screening experiments and successfully isolates CTCs from patient blood samples. The proposed motion controlled microchip-based immunomagnetic system shows great promise as a clinical tool for cancer diagnosis and prognosis.

Keywords Circulating tumor cells (CTCs) · Immunomagnetic assay · Microfluidic chip · Gravity · Capture efficiency · Purity · Fluorescent imaging

1 Introduction

Detection of circulating tumor cells (CTCs) in blood can potentially reveal crucial information about cancer biology. Separation of rare CTCs from whole blood samples is gaining considerable attention in studying cancer biology (Uhr and Pantel 2011). CTCs can be important indicators of metastatic cancer disease (Fehm et al. 2002; Allard et al. 2004; Budd et al. 2006; Paterlini-Brechot and Benali 2007; Mostert et al. 2009; Liu et al. 2009; Bao et al. 2010). Monitoring the response to a treatment couple weeks after initiation of the treatment provides important information for decisions on individualized treatment (Jocelyn 2010). However, isolation of CTCs from whole patient blood samples is challenging due to the rarity of CTCs ($1:10^7$–10^9 blood cells).

Several approaches to developing an effective CTC screening systems, such as CellSearch™ system (Miller et al. 2010), have been proposed to enumerate CTCs. However, CellSearch system's available functionality is still limited only to enumeration of cells suspended in liquid, and it is not straightforward to further track and analyze individual cells. Various microfluidic devices have been developed for isolating rare cells, including CTCs. Microfluidic devices with antibody-coated microstructures for target rare cells are proposed (Nagrath et al. 2007; Talasaza et al. 2009; Stott

Y.-y. Huang · K. Hoshino · P. Chen · C.-h. Wu · J. X. Zhang (✉)
Department of Biomedical Engineering,
The University of Texas at Austin,
University Station, C0800, Austin, TX 78712-0238, USA
e-mail: john.zhang@engr.utexas.edu

N. Lane · M. Huebschman · H. Liu · J. W. Uhr · E. P. Frenkel
Harold C. Simons Comprehensive Cancer Center of the University of Texas Southwestern, Medical Center, USA,
5323 Harry Hines Boulevard,
Dallas, TX 7390-852, USA

K. Sokolov
Department of Imaging Physics, Division of Diagnostic Imaging,
The University of Texas MD Anderson Cancer Center,
1515 Holcombe Blvd,
Houston, TX 77030, USA

et al. 2010; Hosokawa et al. 2010; Sun et al. 2012). Some devices are based on differences in cell size (Bhagat et al. 2011; Hur et al. 2011; Zhang et al. 2011). Recently, microfluidic devices integrated with magnetic carriers are proposed for the enrichment of CTCs (Yung et al. 2009; Estes et al. 2009; Kang et al. 2012; Zhu et al. 2012; Hossain et al. 2012). Integration of an immunomagnetic assay and a microfluidic chip precisely controls screening process by utilizing miniaturized immunomagnetic techniques inside microchannels for efficient isolation of magnetic nanoparticle-labeled cells.

Here we introduce an automated motion-controlled microfluidic system for immunomagnetic detection of CTCs. Based on the screening system we previously developed for spiked screening experiments (Hoshino et al. 2011), we optimize magnetic field distribution by smoothening magnetic gradient within the microchannel. A spacer is inserted between the microchannel and the permanent magnets close to the front end of microchannel to reduce magnetic force near the inlet, eliminating aggregation of nanoparticles. We retain direct contact between magnets and microchannel to have a stronger magnetic field at the rear end of microchannel, aiming to capture all cells that escape weaker magnetic field near the inlet. As a whole, particles can be distributed evenly on the CTC capture plane. Moreover, we introduce here the flip-flop automated motion control system that can dynamically change the orientation of microchannel. According to our theoretical investigation, blood sedimentation in the microchannel plays a critical role in affecting capture efficiency, throughput, and purity of the system (Hoshino et al. 2012). Therefore, by dynamically modifying the orientations of microchannel, the negative effects of blood stagnation, such as mechanical interference and non-specific bindings, can be minimized. The rotational holder is computer-controlled, placing microchannels in an inverted or upright position according to different requirements from different screening steps. After screening, CTCs are permanently fixed on a glass coverslip surface. Cells being permanently fixed on glass substrate are beneficial for future track and further analysis, such as fluorescence *in situ* hybridization (FISH) analysis and hyperspectral microscopic imaging (HMI) analysis (Sieben et al. 2007; Shaffer et al. 2007; Swennenhuis et al. 2009; Leversha et al. 2009).

2 Materials and methods

2.1 Design and fabrication of microchip-based immunomagnetic system

Schematic of the microchip-based immunomagnetic isolation system is shown in Fig. 1. A polydimethylsiloxane (PDMS) microchannel bonded to a glass coverslip is

Fig. 1 PDMS microchip design for immunomagnetic isolation of cancer cells. Magnets are put on top of the microchannel (inverted channel) during the whole screening process. (a) Schematic illustration of the principle of operation of the inverted microchip. Magnetic nanoparticle-labeled CTCs are captured to the microchannel substrate by the magnetic field as the blood sample flows through the microchannel. Gravity force drags blood cells to the opposite side of the microchannel substrate. (b) A spacer, which is placed between the magnets and microchannel, is introduced to create magnetic field gradient increasing throughout the whole microchannel. (c) Top view of a microchannel and permanent magnets. (d) Top view of a microchannel and permanent magnets together with a spacer
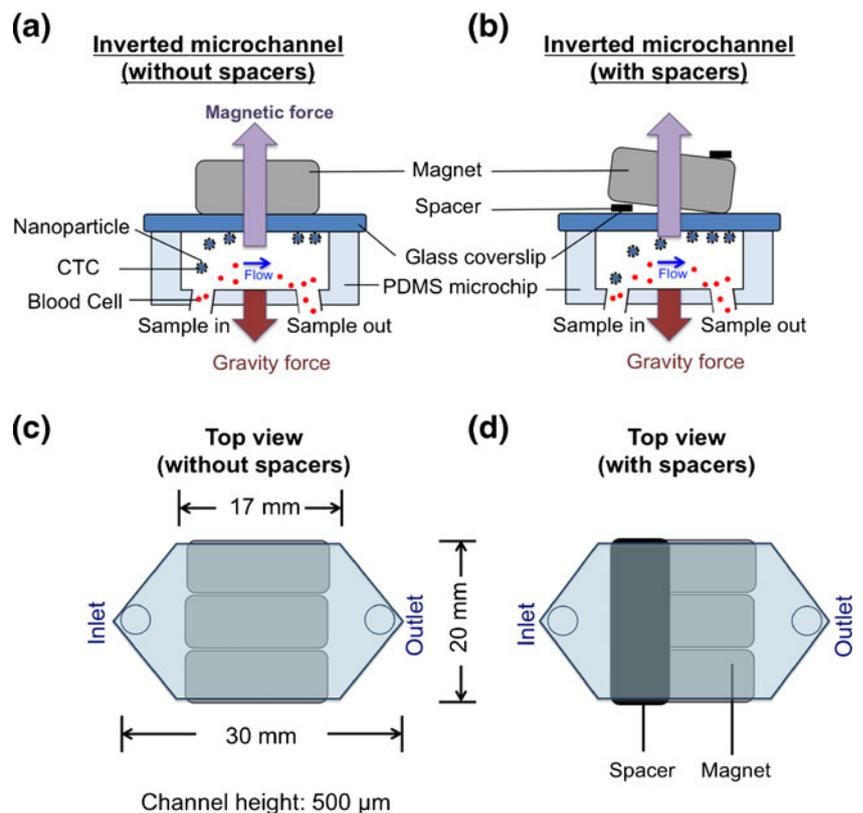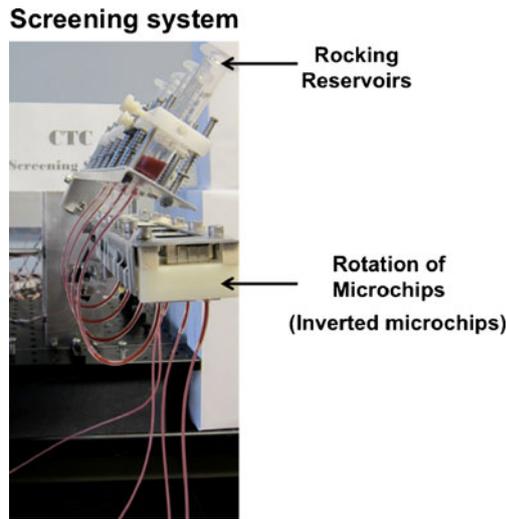
Screening system

Fig. 2 Automated screening system for parallel screening, rotation of microchips, and rock of reservoirs

used as a chamber through which blood sample flows. Target cancer cells are labeled with commercial Fe_3O_4 magnetic nanoparticles (Veridex Ferrofluid™, LLC), which are functionalized with anti-epithelial cell adhesion molecules (anti-EpCAM). As the blood sample flows through the microchannel on top of an array of permanent magnets, nanoparticle-labeled cancer cells are separated from blood flow and are captured on the substrate of the microchannel. Glass slides with captured cancer cells are then detached from the PDMS microchannel and fluorescently stained with DAPI, anti-cytokeratin, and anti-CD45. Subsequently, fluorescence images of captured and stained cancer cells are taken and used for cancer cell identification by trained observers based on fluorescence intensities and cell morphological information. An array of magnets (Block NdFeB magnet, product of 42 MGOe, grade N42, 3/4″ × 1/2″ × 7/32″, magnetized through 3/4″) with opposite polarities next to each other is placed outside the channel on top of the glass substrate in the inverted microchip. Figure 1(a) shows the operation of the microchip-based screening system. A 1 mm thick spacer (elastic sheet magnet, which sizes 10 mm ×20 mm ×1 mm) is introduced at the front end of the microchannel between the magnets and the microchannel, as shown in Fig. 1(b). Figure 1(c) shows the top view of the microchip-based screening system without any spacers. Dimensions of the microchip are also shown in Fig. 1(c). The top view of the microchip together with a spacer is shown in Fig. 1(d). Aggregation of nanoparticles interferes with the identification process by burying the CTCs, making them invisible, or even damaging them. Using a compact system of a spacer and a permanent magnet array, we created a smooth magnetic gradient distribution across the microchannel. Strong magnetic field gradient

Fig. 3 Magnetic field distribution in the microchannel, calculated using COMSOL. (a) Magnetic field distribution of three parallel magnets with a spacer. (b) Magnetic flux densities at different locations across the channel (lines 1, 2, and 3) at the height of 200 μm in the microchannel. (c) Magnetic field distribution of permanent magnets without spacers. (d) Plots of magnetic flux densities at the top and bottom of the microchannel
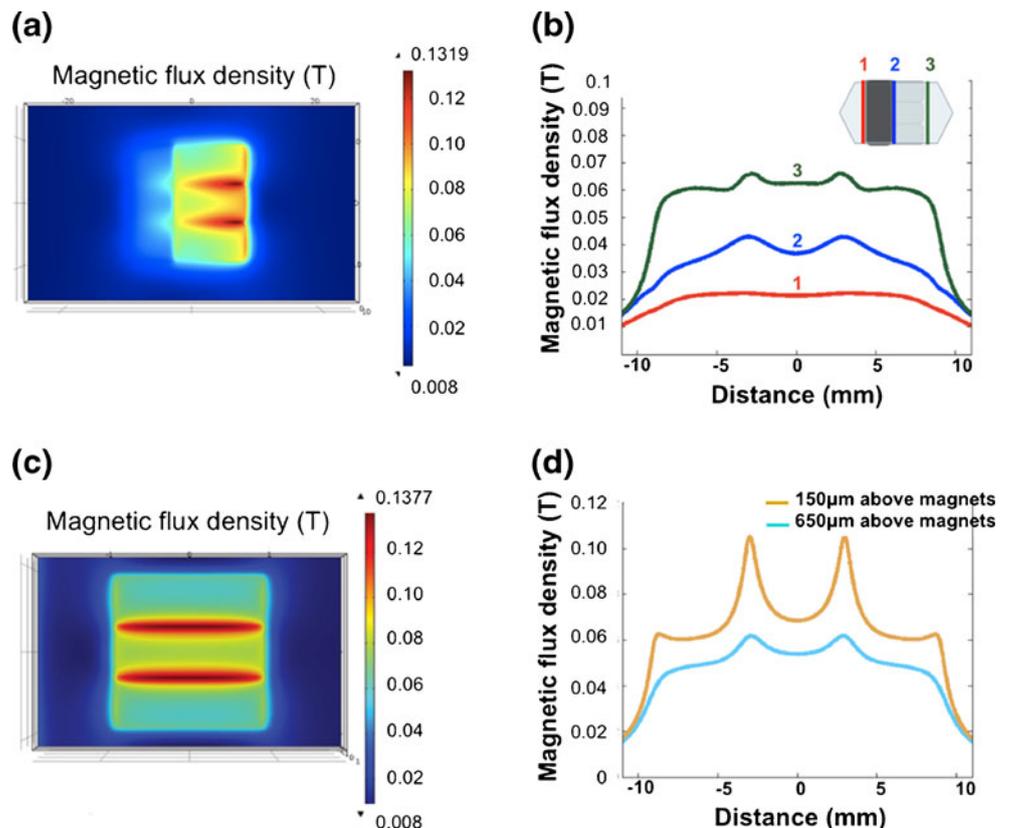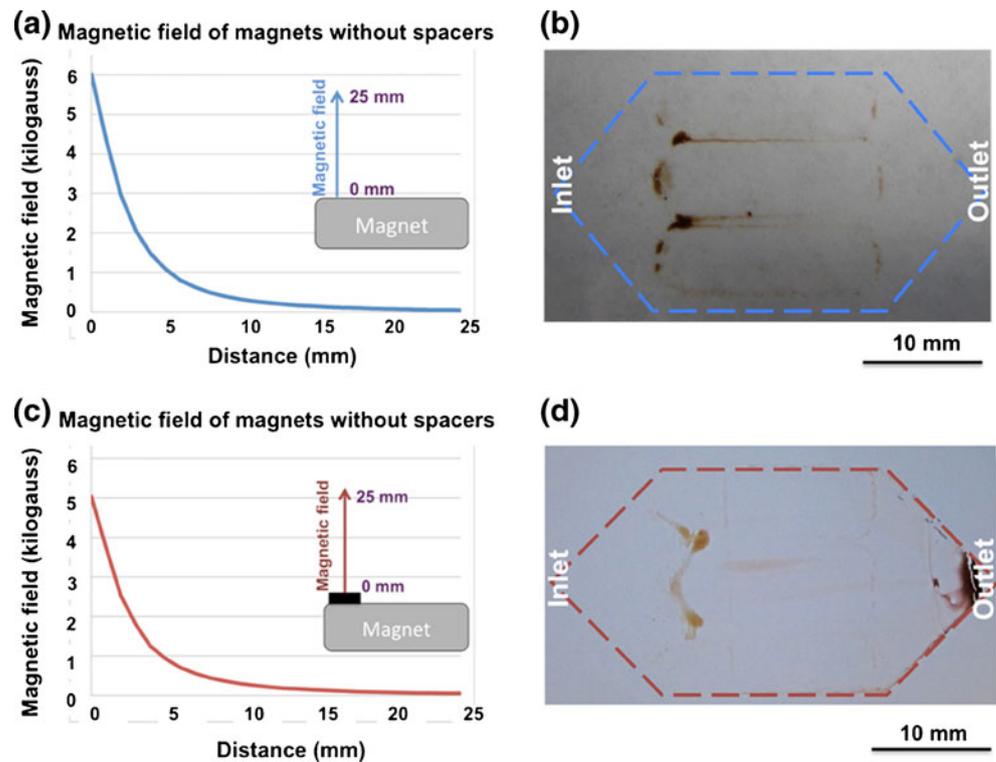
Fig. 4 (**a**) Measured magnetic field of a permanent magnet without any spacers. (**b**) More nanoparticles aggregate close to the front end of the glass coverslip when no spacers was induced. (**c**) Measured magnetic field of a permanent magnet together with a spacer. (**d**) Less nanoparticles aggregate in the front end of the glass coverslip

rather than absolute magnetic field strength is required for effective attraction of magnetic nanoparticles, which function as small magnetic dipoles. Target nanoparticle-labeled CTCs and free nanoparticles experience a smaller magnetic field in the first half of the microchannel and gradually flow to the area with a stronger magnetic field at the other end near the outlet. This design avoids nanoparticle aggregation that interferes with subsequent immunofluorescence observation. The clinical blood sample, containing CTCs expressing EpCAM, is mixed with magnetic nanoparticles conjugated with anti-EpCAM to label target CTCs. The size of Fe_3O_4 particles (Veridex Ferrofluid) is of the order of 100 nm. The microchannel is made by bonding a PDMS channel (Sylgard184, Dow Corning, Midland, MI, 10:1 prepolymer to curing agent) with a 150 μm thick glass coverslip. A standard syringe pump (Harvard apparatus, PHD IW with 6×10 rack) is attached to the outlet of the PDMS microchip through tubing and used to draw blood sample with a syringe. The reservoir, which is held higher than the microchip, is connected to the inlet through tubing.

We developed an automatic rotational microchip holder, which is comprised of DC motors and optical position sensors. Figure 2 shows the developed screening system. A LabView program is used to control the position of the rotating arm. The system is able to dynamically rotate the orientation of the microfluidic chips to keep them operated in the best orientation. The system can also rock the

reservoir to keep blood sample mixed during the screening experiments. The screening system is capable of screening up to six samples simultaneously.

2.2 Magnetic field distribution

We used a gauss meter to measure the magnetic field of one magnet, and used the measured values to define parameters in the simulation and calculate the result of three magnets arranged with opposite polarities next to each other. We used COMSOL for the magnetic field simulation. Figure 3(a) plots the magnetic field flux density distribution for a plane 200 μm away from the bottom substrate of the microchannel calculated using commercial finite element method (FEM) software COMSOL. In order to demonstrate our idea of smoothening the magnetic field gradient by adding spacers, we compared the magnetic flux densities at three different sites (Lines 1, 2, and 3 in the inset of Fig. 3(b)) over the channel. It is observed that the spacer decreases the magnetic field, reducing the gradient, and thus reducing the magnetic force acting on nanoparticles in the

Table 1 Measurement results of viscosities of different RBC volumetric concentration

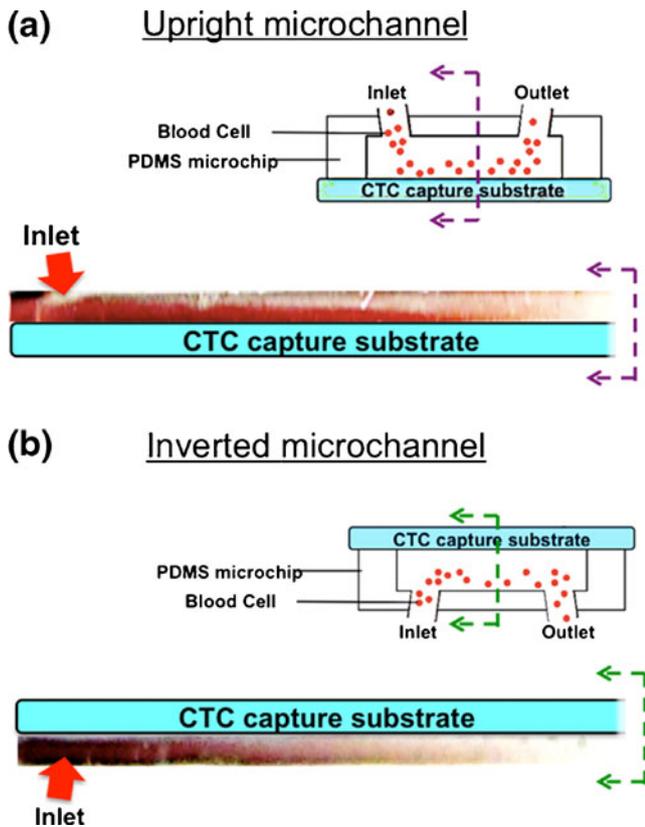| Red blood cell volumetric concentration	50	25	12.5	6.3	3.1
Viscosity (cP)	18.4	15.3	6.13	7.15	5.11

Fig. 5 Experimental photos of blood sedimentation in microchip of a flip flop operation. (a) Sedimentation layer of RBCs is on the CTC capture substrate that acts as a barrier for the capture of CTC in the upright channel. (b) RBC sedimentation layer covers the opposite plane of the CTC capture substrate that target CTCs experience less viscous force by the RBCs to be captured on the CTC capture substrate

microchannel. Magnetic field flux density distribution for a plane 200 μm away from the channel substrate with no spacers placed on top of the magnets is shown in Fig. 3(c). Moreover, in order to prove that the cells will be captured onto the surface of the microchannel, we compare the magnetic flux density at the bottom and top of the channel as shown in Fig. 3(d).

2.3 Flow of red blood cell in the microchannel

The details of the calculation method (sedimentation model and viscosity model) are described in our previous
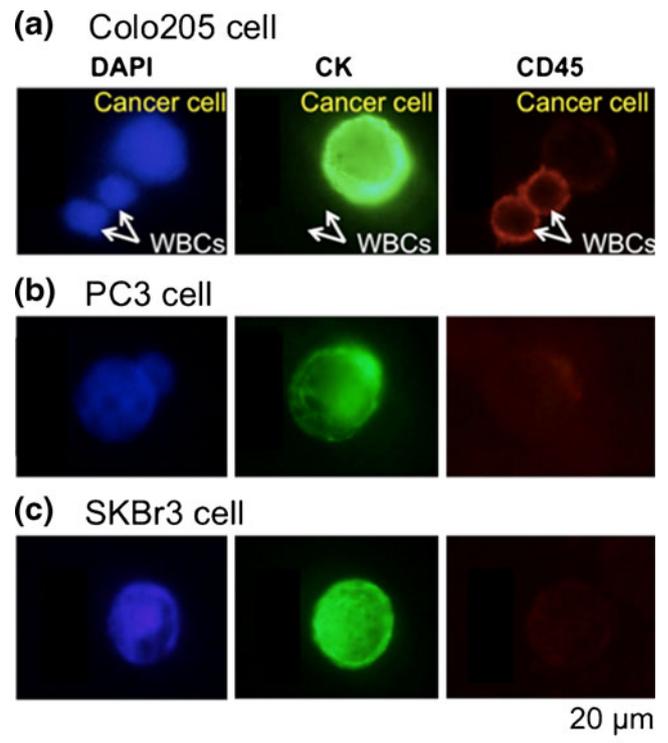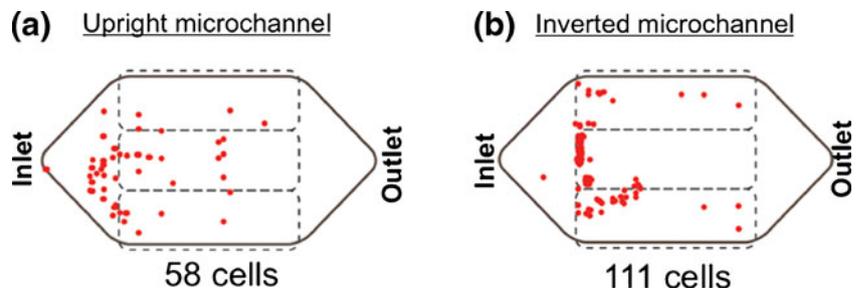

Fig. 7 Fluorescence images of captured cancer cells and WBCs. (a) Examples of DAPI (blue, positive), CK (green, positive), and CD45 (red, negative) fluorescence images of a captured Colo205 cell along with DAPI (blue, positive), CK (green, negative), and CD45 (red, positive) fluorescence images of two WBCs. (b) Fluorescence images of a captured PC3 (prostate cancer cell line). (c) Fluorescence images of a captured SkBr3 (breast cancer cell line)

publication (Hoshino et al. 2012). In brief, the channel space is divided into multiple cubic control volumes. The RBC volumetric concentration in each control volume is updated for each time step based on RBC fluxes from adjacent control volumes. Based on the experimental measurement, a linear relation between the RBC concentration and local viscosity is established to calculate the local viscosity in each control volume.

2.4 Sample preparation

Blood samples, which were collected in CellSave™ tubes (Veridex, LLC, NJ) and EDTA tubes, from the University of

Fig. 6 Map of spiked cancer cells (Colo205 cells) on the glass coverslip. (a) On the upright channel, less cancer cells (58 cells) were found. (b) More cancer cells (111 cells) were captured by the inverted channel

Texas Southwestern Medical Center were separated into conical tubes, each with 2.5 mL of blood sample. Blood plasma was then replaced with dilution buffer solution (Veridex, LLC). A suspension of anti-EpCAM functionalized Fe_3O_4 magnetic nanoparticles and capture enhancement reagent (Veridex, LLC) were added into each conical tube and incubated in a strong magnetic field. Subsequently, blood samples were screened by the developed system.

Colo205 (colon cell line), PC3 (prostate cell line) and SkBr3 (breast cell line) were used for spiked experiments to characterize the capture efficiency of the developed screening system. A solution with approximately 200 cells (100 µL cell suspension) was spiked into 2.5 mL aliquot of blood sample. The same amount of cell suspension (100 µL) was dropped on two glass slides and used as control samples. The capture rate is calculated by dividing the number of cells that are actually spiked into the screening sample by the average number of cells on two control glass slides.

2.5 Separation process

A syringe pump was used to draw the blood sample from the reservoir into the microchannel for the separation process. Flow rate was 2.5 mL/h. After the separation step, phosphate buffered saline (PBS) was introduced into the microchannel for the flushing step to remove unwanted cells, including RBCs, white blood cells (WBCs), and non-target cells, from the glass coverslip. Next, captured nanoparticle-labeled CTCs were fixed on the glass coverslip permanently using cold acetone while cooling down the microchip in the ice bath. After peeling the PDMS microchip off the glass coverslip, the sample slide was stored at 4°C before the following identification process.

2.6 Identification process

The sample slides were immunofluorecently stained with DAPI (used to stain DNA in cell nucleus), anti-cytokeratin (used to stain protein in epithelial tissue) and anti-CD45 (expressed on leukocytes). Captured CTCs show positive DAPI, positive CK, and negative CD45. More details about the staining step and identification step are described in (Hoshino et al. 2011).

3 Results and discussion

3.1 Measured magnetic field

Figure 4(a) shows the measured magnetic field induced by a permanent magnet without any spacers. A distribution of nanoparticles on the channel substrate after the screening is shown in Fig. 4(b). Many particles
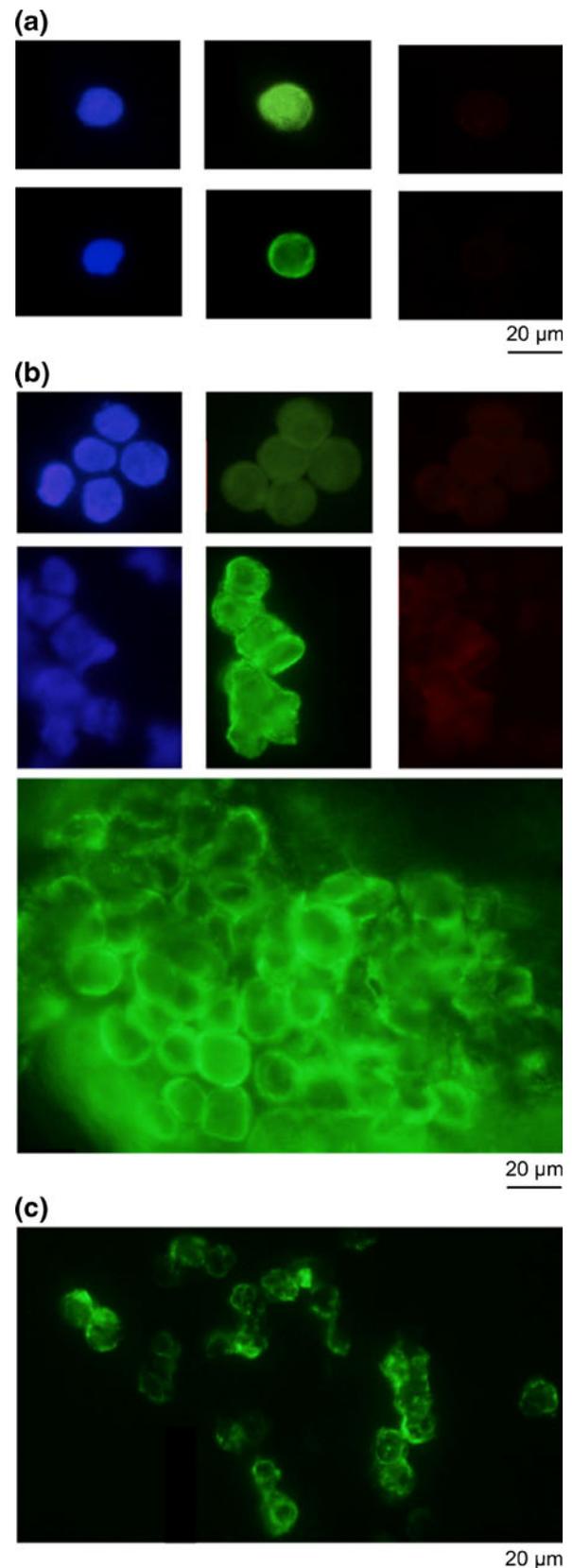

Fig. 8 Fluorescence images of captured CTCs from patient samples. (a) Singlet CTCs isolated from patient samples. (b) Clusters of CTCs separated from patient samples. (c) Clusters of CTCs from a patient sample

were aggregated on the glass coverslip along the strong magnetic field. Figure 4(c) shows the measured magnetic field of a permanent magnet attached with a spacer. With the spacer, fewer nanoparticle aggregates can be seen in the front end of the microchip, as shown in Fig. 4(d).

3.2 Viscosity measurement of RBCs

We performed experimental measurements to calibrate the relation between the RBC volumetric concentration and local viscosity, using a cone plate viscometer (DV-I+, Brookefield, Middleboro, MA). The shear rate we used for the measurement was $2s^{-1}$. The results are shown in Table 1. Obviously, the viscosity is direct proportional to the RBC volumetric concentration, with an approximately linear relationship.

3.3 Blood sedimentation experiments

Figure 5 shows the experimental results of RBC sedimentation in the upright channel and the inverted channel. The microchannel was filled with PBS followed by the introduction of RBCs suspension. The flow rate was set to be 10 mL/h. With the upright channel, RBC sedimentation covers the bottom substrate, which is the CTC capture substrate. It is observed that the substrate is being covered by the layer of RBCs, as shown in Fig. 5(a), in the upright case. Figure 5(b) shows RBCs settle down on the opposite plane of the CTC capture substrate in the inverted channel. Therefore, in the upright channel, RBCs sedimentation on the CTC capture substrate acts as a barrier layer for target cells to be captured on the substrate. Compared to the upright channel, nanoparticle-labeled target cells can be easily attracted to the channel substrate in the inverted channel.

3.4 The spiked sample experiments

The positions of the captured cells on the glass substrate are also shown in Fig. 6. On the upright channel (Fig. 6 (a)), 58 cells were found on the coverslip while on the inverted channel, more cancer cells (111 cells) were found on the coverslip (Fig. 6(b)). As we discussed above, this resulted from the blood cell's sedimentation impact on cancer cell separation. Due to high viscous layer covering the substrate in the upright channel, it is more difficult for cancer cells to get close to and finally be captured onto the channel substrate. Therefore, more cells are captured on the channel substrate of the inverted channel in comparison to the cells captured on the substrate of the upright channel.

For the assessment of number of cancer cells nonselectively stays on the channel substrate, a blood sample was spiked with approximately 100,000 cancer cells for a screening experiment without any permanent magnets placed under the microchip. The screened result showed that no cancer cell was found from the channel substrate. The developed system proves the high selectivity (Hoshino et al. 2011).

Figure 7(a) shows the fluorescence images of a captured Colo205 along with two WBCs from the spiked screening experiment. Fluorescence images of captured PC3 and SkBr3 are also shown in Fig. 7(b) and (c), respectively.

Using the screening system for the spiked experiments, the average capture rates for SkBr3, PC3 and Colo205 cells were 97%, 107% and 94%, respectively. Capture rates could be more than 100% when the number of cells added to the spiked sample is more than the number of cells prepared for the control samples due to concentration variations in small sampling aliquots.

Table 2 Summary of patient samples and CTC counts of blood samples from cancer patients (pathology information included)

Sample number	Ferrofluid/blood (μL/mL)	Flow rate (mL/h)	Screen volume (mL)	Number of CTCs	Gender	Cancertype	Numbers of CTCs/ 7.5mL (Microchip)	Numbers of CTCs/ 7.5mL (CellSearch)
1	7.5	2.5	5	30	F	Breast cancer	20	16
2	7.5	2.5	10	50	F	Breast cancer	33	10
3	7.5	2.5	5	1	M	Prostate cancer	0.6	3
4	7.5	2.5	5	1	F	Lung Cancer	0.6	N/A
5	7.5	2.5	5	1	F	Lung Cancer	0.6	N/A
6	7.5	2.5	7.5	5	F	Breast cancer	3	N/A
7	7.5	2.5	5	19	F	Breast cancer	13	N/A
8	7.5	2.5	5	28	F	Lung Cancer	19	N/A
9	7.5	2.5	5	>1,000	F	Breast cancer	>666	N/A
10	7.5	2.5	7.5	1	F	Breast cancer	0.6	N/A
11	7.5	2.5	7.5	1	F	Breast cancer	0.6	N/A

3.5 Patient studies

The system was applied to the clinical study of isolating CTCs from patient samples. CTCs were successfully isolated from patients' blood samples with a variety of types of cancer. Figure 8 shows immunofluorescence images of captured CTCs separated from clinical samples. Figure 8(a) shows a single CTC found from two patient samples. Table 2 shows the numbers of CTCs found from screened subject samples in which CTCs were captured by the microchip. Samples number 1 and 2 were screened with the commercial CellSearch screening system in parallel with our microchip-based screening system for evaluation. Our system had comparable capture rates with the CellSearch system. In addition, we were able to find clusters of CTCs in clinical samples (Fig. 8(b)). Clusters of CTCs could detach from the proliferation of intravascular cancer cells (Al-Mehdi et al. 2000). A cluster of 50 CTCs was captured from patient sample number 2, a blood sample from a female subject with breast cancer disease. More than a thousand CTCs were found from the patient sample number 9 (Fig. 8(c)), who had a stage 4 lung cancer. Unlike spiked cancer cells (see Fig. 7), CTCs separated from clinical samples vary in size, shape, and CK expression level. Cancer cells in Fig. 8 (c) also shows lower level of CK comparing to the higher CK level of spiked cancer cells in Fig. 7. Cultured cancer cell lines such as PC3, SkBr3 and Colo205 that are commonly used for spiked screening experiments express more EpCAM or Cytokeratin than CTCs from clinical samples since some CTCs are believed to undergo Epithelial Mesenchymal Transition (EMT) while circulating in the blood stream (Uva et al. 2010; Lazar et al. 2012).

4 Conclusion

We have developed a unique immunomagnetic microchip-based flip-flop automated screening system. Surface functionalized magnetic nanoparticles are used to label target cancer cells in the microchip during the blood screening process. Target cancer cells are captured on the flat surface of a glass substrate making it beneficial for the identification process. We optimized the magnetic field distribution by reducing the magnetic force close to the front end of the microchannel thus reducing the nanoparticle aggregation close to the inlet. In particular, the flip-flop dynamic system can change the orientation of the microchip reducing the stagnation of RBCs and non-specific binding on the capture surface.

With the optimized conditions of the screening system, captured rates of more than 90% were demonstrated for blood samples spiked with SkBr3, PC3, and Colo205 cells. The screening system successfully isolated CTCs from the blood samples of cancer patients. Efficient capturing of CTCs has been demonstrated, while the rare cells were fixed on the coverslip after screening for further biological and imaging analysis. Different types of CTCs were observed from patient blood samples. Many clusters of CTCs were isolated from patient blood samples. The proposed motion controlled microchip-based immunomagnetic system shows great promise as a tool for cancer prognosis.

References

J.W. Uhr, K. Pantel, PNAS **108**, 12396–12400 (2011)

T. Fehm, A. Sagalowsky, E. Clifford, P. Beitsch, H. Saboorian, D. Euhus, S. Meng, L. Morrison, T. Tucker, N. Lane, B.M. Ghadimi, K. Heselmeyer-Haddad, T. Ried, C. Rao, J.W. Uhr, Clin. Cancer Res. **8**, 2073–2084 (2002)

W.J. Allard, J. Matera, M.C. Miller, M. Repollet, M.C. Connelly, C. Rao, A.G.J. Tibbe, J.W. Uhr, L.W. Terstappen, Clin. Cancer Res. **10**, 6897–6904 (2004)

G.T. Budd, M. Cristofanilli, M.J. Ellis, A. Stopeck, E. Borden, M.C. Miller, J. Matera, M. Repollet, G.V. Doyle, L.W.M.M. Terstappen, D.F. Hayes, Clin. Cancer Res. **12**, 6403–6409 (2006)

P. Paterlini-Brechot, N.L. Benali, Science **253**, 180–204 (2007)

B. Mostert, S. Sleijfer, J.A. Foekens, J.W.S. Gratama, Cancer Treat Rev **35**, 463–474 (2009)

M.C. Liu, P.G. Shields, R.D. Warren, P. Cohen, M. Wilkinson, Y.L. Ottaviano, S.B. Rao, J. Eng-Wong, F. Seillier-Moiseiwitsch, A.M. Noone, C. Isaacs, J. Clin. Oncol. **27**, 5153–5159 (2009)

N. Bao, T.T. Le, J.X. Cheng, C. Lu, Integr. Biol. **2**, 113–120 (2010)

K. Jocelyn, Science **327**, 1072–1074 (2010)

M.C. Miller, G.V. Doyle, L.W.M.M. Terstappen, Journal of Oncology **2010**, 1–8 (2010)

S. Nagrath, L.V. Sequist, S. Maheswaran, D.W. Bell, D. Irimia, L. Ulkus, M.R. Smith, E.L. Kwak, S. Digumarthy, A. Muzikansky, P. Ryan, U.J. Balis, R.G. Tompkins, D.A. Haber and M. Toner, 450, pp. 1235–1239 (2007)

A.H. Talasaza, A.A. Powellc, D.E. Huberb, J.G. Berbeeb, K.-H. Rohd, W. Yud, W. Xiaob, M.M. Davisd, R.F. Peasea, M.N. Mindrinosb, S.S. Jeffrey, R.W. Davis, PNAS **106**, 3970–3975 (2009)

S.L. Stott, C.H. Hsu, D.I. Tsukrov, M. Yu, D.T. Miyamoto, B.A. Waltman, S.M. Rothenberg, A.M. Shah, M.E. Smas, G.K. Korir, F.P. Floyd Jr., A.J. Gilman, J.B. Lord, D. Winokur, S. Springer, D. Irimia, S. Nagrath, L.V. Sequist, R.J. Lee, K.J. Isselbacher, S. Maheswaranc, D.A. Haber, M. Toner, PNAS **107**, 18392–18397 (2010)

M. Hosokawa, T. Hayata, Y. Fukuda, A. Arakaki, T. Yoshino, T. Tanaka, T. Matsunaga, Anal. Chem. **82**, 6629–6635 (2010)

J. Sun, M. Li, C. Liu, Y. Zhang, D. Liu, W. Liu, G. Hu, X. Jiang, Lab on a Chip (2012)

A.A. Bhagat, H.W. Hou, L.D. Li, C.T. Lim, J. Han, Lab on a Chip **11**, 1870–1878 (2011)

S.C. Hur, A.J. Mach, D.D. Carlo, AIP Biomicrofluidics **5**, 022206 (2011)

S. Zhang, H.K. Lin, and B. Lu, Biomed Microdevices, pp. 203–213 (2011)

C.W. Yung, J. Fiering, A.J. Mueller, D.E. Ingber, Lab on a Chip **9**, 1171–1177 (2009)

M.D. Estes, B. Ouyang, S.M. Ho, C.H. Ahn, J. Micromech. Microeng. **19**, 095015 (2009)

J.H. Kang, S. Krause, H. Tobin, A. Mammoto, M. Kanapathipillai, D.E. Ingber, Lab on a Chip **12**, 2175–2181 (2012)

T. Zhu, R. Cheng, S.A. Lee, E. Rajaraman, M.A. Eiteman, T.D. Querec, E.R. Unger, L. Mao, Microfluid Nnaofluid (2012)

M. Hossain, Y. Luo, Z. Sun, C. Wang, M. Zhang, H. Fu, Y. Qiao, M. Su, Biosens. Bioelectron. **1**, 348–354 (2012)

K. Hoshino, Y.Y. Huang, N. Lane, M. Huebhman, J.W. Uhr, E.P. Frenkel, X.J. Zhang, Lab on a Chip **11**, 3449–3457 (2011)

K. Hoshino, P. Chen, Y.Y. Huang, X.J. Zhang, J. Anal. Chem. **10**, 4292–4299 (2012)

V.J. Sieben, C.S. Debes Marun, P.M. Pilarski, G.V. Kaigala, L.M. Pilarski, C.J. Backhouse, IET Nanobiotechnol **1**, 27–35 (2007)

D.R. Shaffer, M.A. Leversha, D.C. Danila, O. Lin, R. Gonzalez-Espinoza, B. Gu, A. Anand, K. Smith, P. Maslak, G.V. Doyle, L.W.M.M. Terstappen, H. Lilja, G. Heller, M. Fleisher, H.I. Scher, Clin. Cancer Res. **13**, 2023–2029 (2007)

J.F. Swennenhuis, A.G. Tibbe, R. Levink, R.C. Sipkema, L.W. Terstappen, Cytometry A **75**, 520–527 (2009)

M.A. Leversha, J. Han, Z. Asgari, D.C. Danila, O. Lin, R. Gonzalez-Espinoza, A. Anand, H. Lilja, G. Heller, M. Fleisher, H.I. Scher, Clin. Cancer Res. **15**, 2091–2097 (2009)

A.B. Al-Mehdi, K. Tozawa, A.B. Fisher, L. Shientag, A. Lee, R.J. Muschel, Nat. Med. **6**, 100–102 (2000)

P. Uva, A. Lahm, A. Sbardellati, A. Grigoriadis, T. Andrew, E.D. Rinaldis, PLoS One **5**, 11 (2010)

D.C. Lazar, E.H. Cho, M.S. Luttgen, T.J. Metzner, M.L. Uson, M. Torrey, M.E. Gross, P. Kuhn, Phys. Biol. **9**, 7 (2012)